CELL BIOLOGY

Extracellular matrix stiffness determines DNA repair efficiency and cellular sensitivity to genotoxic agents

Min Deng[1]*[†], Jing Lin[2]*, Somaira Nowsheen[1], Tongzheng Liu[3], Yingchun Zhao[4], Peter W. Villalta[4], Delphine Sicard[5], Daniel J. Tschumperlin[5], SeungBaek Lee[6], JungJin Kim[6], Zhenkun Lou[1][†]

DNA double-strand breaks (DSBs) are highly toxic lesions that can drive genetic instability. These lesions also contribute to the efficacy of radiotherapy and many cancer chemotherapeutics. DNA repair efficiency is regulated by both intracellular and extracellular chemical signals. However, it is largely unknown whether this process is regulated by physical stimuli such as extracellular mechanical signals. Here, we report that DSB repair is regulated by extracellular mechanical signals. Low extracellular matrix (ECM) stiffness impairs DSB repair and renders cells sensitive to genotoxic agents. Mechanistically, we found that the MAP4K4/6/7 kinases are activated and phosphorylate ubiquitin in cells at low stiffness. Phosphorylated ubiquitin impairs RNF8-mediated ubiquitin signaling at DSB sites, leading to DSB repair deficiency. Our results thus demonstrate that ECM stiffness regulates DSB repair efficiency and genotoxic sensitivity through MAP4K4/6/7 kinase–mediated ubiquitin phosphorylation, providing a previously unidentified regulation in DSB-induced ubiquitin signaling.

INTRODUCTION

DNA double-strand breaks (DSBs) pose a potent threat to genomic integrity (*1*). Unrepaired DSBs cause genomic instability and cellular transformation. The capability to repair DSBs also contributes to the efficacy of radiotherapy and many cancer chemotherapeutics. The DSB elicits a signaling cascade that modifies the chromatin surrounding the break, first by ataxia telangiectasia mutated (ATM) kinase–dependent phosphorylation of the histone H2AX (*2–4*) and recruitment of mediator of DNA damage checkpoint protein 1 (MDC1) (*5–7*), followed by ring finger protein 8 (RNF8)– and ring finger protein 168 (RNF168)-dependent regulatory ubiquitination (*8–10*). The DSB-induced ubiquitination cascade is initiated by the RNF8-dependent conjugation of ubiquitin (*10–12*), which promotes the accumulation of RNF168. RNF8 and RNF168 cooperate to catalyze the formation of K63-linked ubiquitin (Ub) chains on chromatin-bound substrates that include histones H2A and H2AX (*8, 9, 13*). This regulatory ubiquitination event promotes the independent recruitment of the receptor-associated protein 80 (RAP80)–BRCA1 complex and TP53-binding protein 1 (53BP1) to the damaged chromatin (*14–17*), which are critical for DSB repair and the G_2-M checkpoint. Deficiency of ubiquitination in the DSB response leads to impaired DSB repair and enhanced sensitivity of tumor cells to genotoxic agents, such as ionizing radiation (IR) and chemotherapy.

Signaling from the extracellular matrix (ECM) is a fundamental cellular input that sustains proliferation, opposes cell death, and regulates differentiation (*18*). Through integrins, cells perceive both the chemical composition and physical properties of the ECM (*19, 20*). In particular, cell behavior is profoundly influenced by the mechanical elasticity or stiffness of the ECM, which regulates the ability of cells to develop forces through their contractile actomyosin cytoskeleton and to mature focal adhesions. This mechanosensing ability affects fundamental cellular functions such that alterations of ECM stiffness are nowadays considered to be not only a simple consequence of pathology but also a causative input driving aberrant cellular behavior. For example, ECM stiffness can regulate YAP/TAZ (yes1 associated transcriptional regulator/transcriptional coactivator with PDZ-binding motif)–mediated transcription through RAP2. At low stiffness, active RAP2 binds to and stimulates the kinases MST1/2 and MAP4K, resulting in activation of large tumor suppressor kinase 1 (LATS1) and LATS2 and inhibition of YAP and TAZ (*21, 22*).

Tissue-level matrix stiffness ranges from elastic modulus E_{brain} ~ 0.1 to 1 kPa to E_{muscle} ~ 8 to 17 kPa to $E_{osteoid}$ ~ 25 to 40 kPa (*23, 24*). While the effects of stiffness on tumor progression are extensively studied (*25, 26*), it is largely unknown whether ECM stiffness affects DSB repair pathway and chemotherapy.

Here, we demonstrate that ECM stiffness is a key extracellular regulator of the DSB repair pathway. Low stiffness activates the RAP2-MAP4K4/6/7 signaling, which phosphorylates ubiquitin at Thr[66]. The phosphorylated ubiquitin blocks RNF8-mediated ubiquitin chain formation, resulting in deficiency of BRCA1 and 53BP1 recruitment and impaired DSB repair. Thus, ECM stiffness plays a key role in DNA repair and controls cellular sensitivity to genotoxic agents.

RESULTS

Low stiffness impairs the DSB repair process and increases cellular sensitivity to genotoxic agents

We first analyzed the relationship between ECM component and chemotherapy sensitivity in breast cancer. We found that the expression level of several ECM components such as connective tissue growth factor (CTGF), lysyl oxidase (LOX), vascular endothelial growth factor receptor (VEGFR), lysyl oxidase like 2 (LOXL2), and actin alpha 2 (ACTA2) are closely correlated with chemotherapy outcome. As shown in fig. S1 (A to F), high expression of any of these genes or combination of these multiple genes correlated with lower survival rate in patients with chemotherapy treatment but not

[1]Department of Oncology, Mayo Clinic, Rochester, MN 55905, USA. [2]Department of Laboratory Medicine, The Forth Medical Center, Beijing 100048, China. [3]Institute of Tumor Pharmacology, Jinan University, 510632 Guangzhou, China. [4]Analytical Biochemistry Shared Resource at the Masonic Cancer Center, University of Minnesota, Minneapolis, MN 55455, USA. [5]Department of Physiology and Biomedical Engineering, Mayo Clinic, Rochester, MN 55902, USA. [6]Department of Radiology, Mayo Clinic, Rochester, MN 55902, USA.
*These authors contributed equally to this work.
†Corresponding author. Email: deng.min@mayo.edu (M.D.); lou.zhenkun@mayo.edu (Z.L.)

in untreated patients or endocrine-treated patients. As CTGF, LOX, VEGFR, LOXL2, and ACTA2 were correlated with fibrosis and high stiffness (27), we thus questioned whether ECM stiffness might regulate chemotherapy efficiency. To test this possibility, we treated mouse mammary tumor 4 T1 xenograft with LOX inhibitor β-aminopropionitrile (BAPN) to reduce tumor stiffness (28). BAPN treatment markedly sensitized tumor to chemotherapy drug cisplatin (fig. S1, G to I). Furthermore, combination of BAPN and cisplatin also induced much more apoptosis than cisplatin alone (fig. S1J). These results indicate that ECM stiffness might play a direct role in DNA repair regulation.

To find out whether ECM stiffness directly regulates the DSB repair pathway, we monitored DSB repair events in human embryonic kidney–293 (HEK293) cells grown on fibronectin-coated acrylamide hydrogels of varying stiffness from 0.5 to 30 kPa, which match the physiological elasticities of natural tissues and tumor (Fig. 1, A to C) (29–33). We first examined how different stiffness regulates cellular response to genotoxic stress. HEK293 cells were treated with IR, cisplatin, etoposide, or neocarzinostatin (NCS). Cells at low stiffness (0.5 and 1 kPa) exhibited a significantly increased sensitivity to all four genotoxic agents compared to cells grown on high stiffness ECM (10, 20, and 30 kPa; Fig. 1, D to G). We found that cells at low stiffness (0.5 kPa and 1 kPa) exhibited a significantly decreased sensitivity to the cyclin-dependent kinase 4/6 inhibitor Palbociclib (34), suggesting that low stiffness specifically increases cellular sensitivity to DNA damaging agents (Fig. 1H). To further confirm this, we detected the ratio of apoptotic cells at different stiffness after genotoxic treatment. As shown in Fig. 1I, cells at low stiffness (0.5 and 1 kPa) exhibited a significantly increased apoptosis after four genotoxic agents compared to cells grown on high stiffness ECM (10, 20, and 30 kPa). Together, our results indicate that low stiffness affects DNA repair efficiency.

We next assessed the clearance of DNA lesions following IR exposure under different ECM stiffness conditions. We used automated immunofluorescence microscopy to quantify nuclear γ-H2AX foci as a surrogate for unrepaired DNA lesions. In response to IR, we observed a significantly delayed clearance of γ-H2AX foci in cells grown on low stiffness ECM (0.5 and 1 kPa) compared to cells cultured on high stiffness ECM (10, 20, and 30 kPa; Fig. 1J), suggesting delayed DSB repair in cells at low stiffness. To further confirm this result, we monitored DSB in cells by neutral comet assay. In response to IR, we observed a significantly delayed clearance of DSB in cells grown on low stiffness ECM (0.5 and 1 kPa) compared to cells cultured on high stiffness ECM (10, 20, and 30 kPa; Fig. 1K), suggesting delayed DSB repair in cells under low stiffness.

Eukaryotic cells use two major pathways, nonhomologous end joining (NHEJ) and homologous recombination (HR), as well as branches of these pathways, to repair DSBs. To assess DSB repair efficiency, we monitored HR and NHEJ using the DR-GFP and EJ5-GFP reporters. The efficiency of both HR and NHEJ was inhibited in cells at low stiffness (0.5 and 1 kPa; Fig. 1, L and M).

To test whether the effect of stiffness on DSB repair is cell type dependent, we next performed colony formation assay and apoptosis analysis in different cell lines, including U2OS, MDA-MB-231, MCF7, A549 and MCF10A. When grown on low-stiff ECM, all five cell lines showed increased sensitivity to genotoxic agents [U2OS (fig. S2, A and B), MDA-MB-231 (fig. S2, C and D), MCF7 (fig. S2, E and F), A549 (fig. S2, G and H), and MCF10A (fig. S2, I and J)], suggesting that the effect of stiffness on cellular DSB repair is a common mechanism that is shared in different cell types.

To further confirm the effects of stiffness on DNA repair, we used two additional cell culture models to manipulate ECM stiffness. First, we used Matrigel-coated plates (stiff) and gelled Matrigel thick layer (soft) system (fig. S2K). Compared to cells grown on Matrigel-coated plates (stiff), cells grown on gelled Matrigel thick layer (soft) were much more sensitive to genotoxic agents (fig. S2, L and M).

Second, we also used a three-dimensional (3D) culture system with soft or stiff hydrogels (35) to assay the effects of stiffness on DNA repair (ig. S2N). Similar to our 2D culture system, cells grown on soft hydrogel in 3D culture system were more sensitive to genotoxic agents than cells grown on stiff hydrogel (Fig. 2O).

To confirm the effect of stiffness on DNA repair in xenograft models, we used semisynthetic hyaluronan-derived hydrogels (36) (soft, 0.4 kPa; stiff, 9 kPa) to mimic the solid tumor stiffness. ECM stiffness did not affect tumor exposure to chemotherapy, as tumor samples from both gels (0.4 and 9 kPa) showed similar tail moment 6 hours after cisplatin treatment (fig. S2P). With this mouse model, we further checked whether stiffness affects cisplatin sensitivity. As shown in fig. S2 (Q to S), tumors at low stiffness were more sensitive to cisplatin. Furthermore, cisplatin also induced much more apoptosis in tumor under soft ECM than under stiff ECM (fig. S2T), indicating that ECM stiffness affects tumor response to chemotherapy.

Low stiffness inhibits DSB repair at the level of RNF8 in the DSB repair pathway

In the DSB repair process, DSB repair proteins are recruited to the DSB site. This process seems to occur in a step-wise fashion with upstream proteins showing faster kinetics. We sought to pinpoint the step during DSB repair signaling that is sensitive to low stiffness. Low stiffness did not have a marked effect on the earliest steps of DNA damage response, as the foci assembly of γ-H2AX, MDC1, and RNF8 were largely unchanged (Fig. 2, A to C, and fig. S3, A to B). However, the ubiquitin conjugation at the DSB site was blocked in cells at low stiffness (Fig. 2D and fig. S3B). The recruitment of RNF168, 53BP1, and BRCA1 to DNA damage sites was also blocked at low stiffness (Fig. 2, E to G, and fig. S3, C to D). As the recruitment of RNF168, 53BP1, and BRCA1 is dependent on RNF8-mediated ubiquitin signaling, we thus concluded that low stiffness inhibits DSB repair through modulating RNF8-mediated ubiquitin signaling (Fig. 2H).

Inhibition of DSB repair by low stiffness is dependent on Rap2

We next sought to investigate how ECM stiffness affects the RNF8-mediated ubiquitin signaling. It is known that Hippo-YAP pathway is regulated by ECM stiffness (24). Recent studies have demonstrated that the RAP2-Hippo pathway is a direct link between ECM stiffness and intracellular processes. Low stiffness can activate RAP2 and the downstream Hippo kinase MST1/2 and MAP4K4/6/7 kinases (fig. S4A). We thus tested whether Rap2 is involved in DSB repair regulation by quantifying the IR-induced foci. Using Rap2 knockout (KO) cells, we further confirmed the effects of Rap2 in DNA repair inhibition by low stiffness. As shown in fig. S4 (B to J), Rap2 KO cells at low stiffness restored FK2/53BP1/BRCA1 foci. Furthermore, at low stiffness, Rap2 KO cells became more resistant to IR when compared to control cells (fig. S4K), indicating that Rap2 is required for DNA repair inhibition by low stiffness.
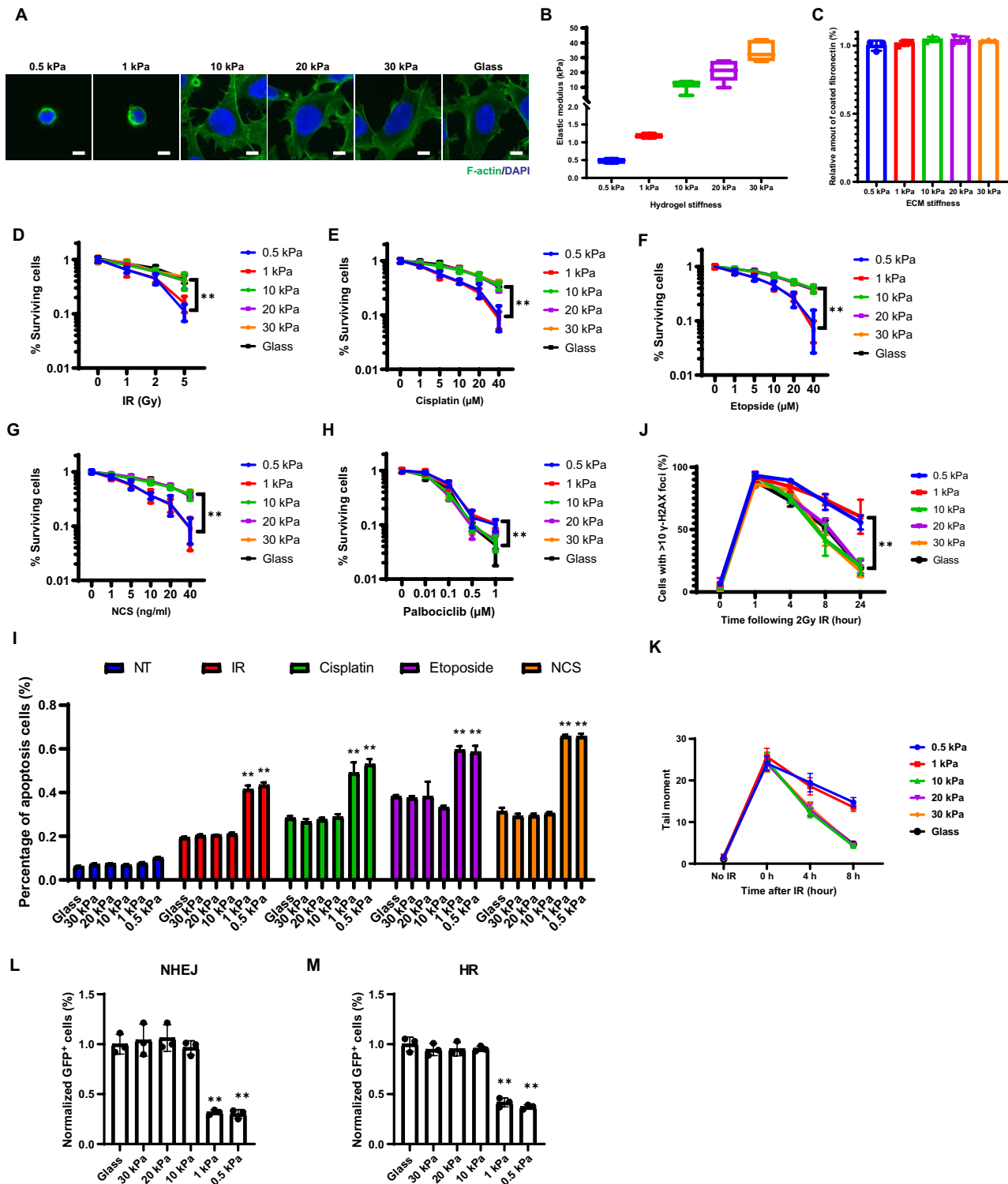
Fig. 1. Low stiffness impairs DSB repair and increases cellular sensitivity to genotoxic agents. (**A**) HEK293 cells grown on different surfaces were stained for F-actin and nucleus. DAPI, 4',6-diamidino-2-phenylindole. (**B**) The elasticity of hydrogels was measured by atomic force microscopy. (**C**) The coating efficiency of fibronectin on hydrogels was measured. (**D** to **H**) HEK293 cells grown on different surfaces were treated with indicated doses of genotoxic agents or Palbociclib. Colony formation assays were performed to detect cell survival. (**I**) HEK293 cells grown on different surfaces were treated with indicated genotoxic agents [10 Gy IR, 10 μM cisplatin, 10 μM etoposide, and NCS (10 ng/ml)]. Cells were trypsinized after 48 hours and cellular apoptosis was detected by annexin V and PI staining. (**J**) HEK293 cells grown on different surfaces were treated with IR (2 Gy) and stained for γ-H2AX at the indicated time points. (**K**) HEK293 cells grown on different surfaces were treated with IR (10 Gy) and harvested at the indicated time points for neutral comet assay. Data are presented as means ± SEM. More than 50 cells per group were quantified (**$P < 0.01$). (**L** and **M**) HEK293 cells with chromosomally integrated HR or NHEJ reporter were plated on different surfaces. The efficiency of NHEJ (L) and HR (M) were analyzed by flow cytometry.
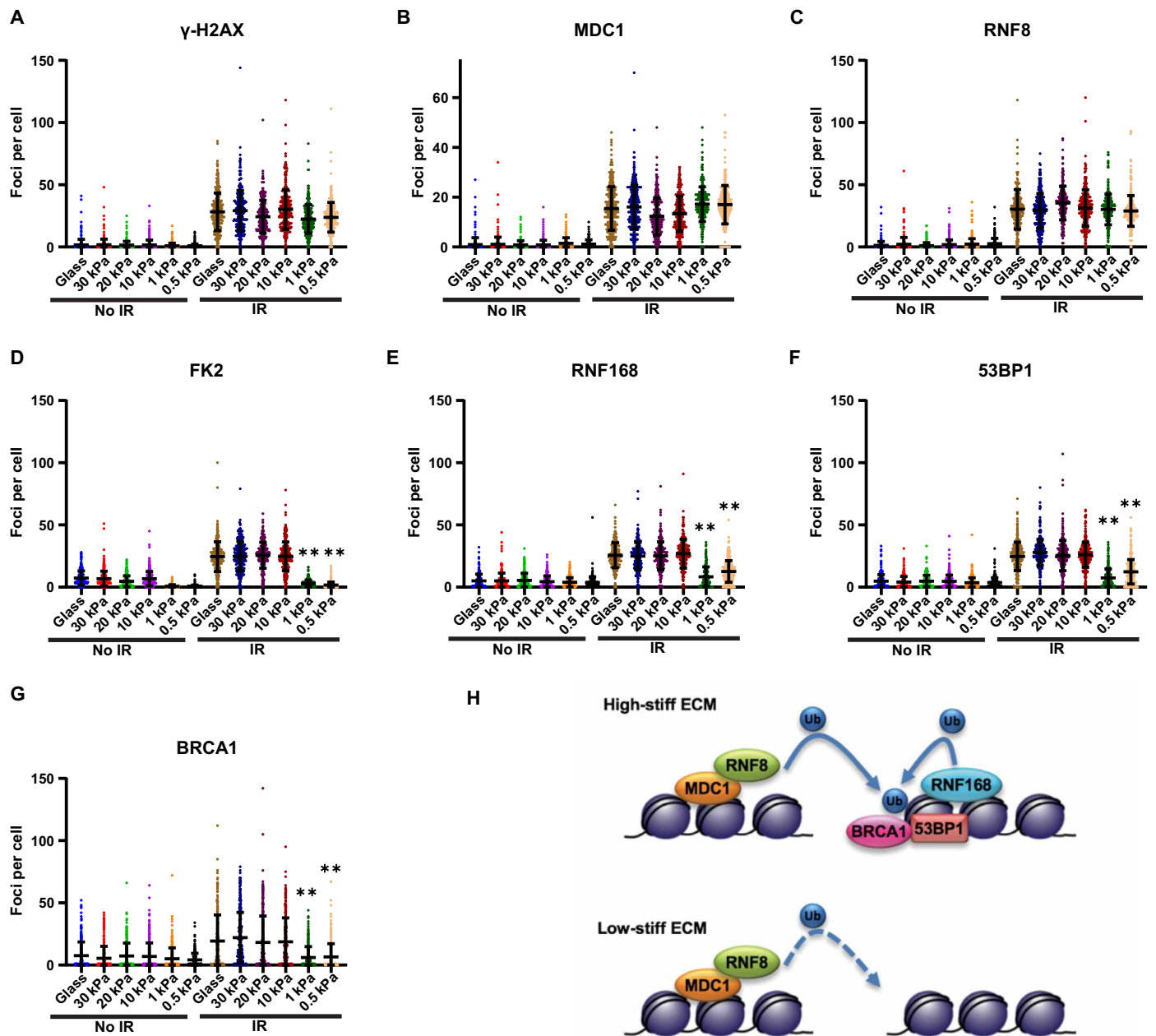
Fig. 2. Low stiffness inhibits DSB repair at the level of RNF8 in the DSB repair pathway. (**A** to **G**) HEK293 cells were grown for 24 hours on fibronectin-coated hydrogels of different stiffness. Cells were fixed 1 hour after irradiation (1 Gy) and stained with anti–γ-H2AX (A), MDC1 (B), RNF8 (C), FK2 (D), 53BP1 (F), and BRCA1(G) antibodies. For RNF168 (E), HEK293 cells expressing mCherry-RNF168 were plated on fibronectin-coated hydrogels of different stiffness. Cells were fixed 1 hour after irradiation (1 Gy), and RNF168 foci were visualized with mCherry. Quantification is described in Methods. Data are presented as means ± SD, $n = 3$ biologically independent samples (**$P < 0.01$). (**H**) A model showing the affected DNA repair steps by low stiffness.

Inhibition of DSB repair by low stiffness is dependent on MAP4K4/6/7

We further tested whether downstream Hippo kinases MST1/2 and MAP4K4/6/7 kinases regulate DNA repair. To test the role of MST1/2 and MAP4K kinases in regulation of DSB repair, we used MST1/2 knockout (MM2KO), MAP4K4/6/7 knockout (MM3KO), and MST1/2 and MAP4K4/6/7 knockout (MM5KO) cell lines to specify the contribution of Hippo kinases to DNA repair regulation (Fig. 3A). At low stiffness, wild-type cells exhibited decreased FK2, 53BP1, and BRCA1 foci at DSB sites. MM3KO and MM5KO cells,

but not MM2KO cells, restored FK2, 53BP1, and BRCA1 foci at low stiffness (Fig. 3, B to J), indicating that MAP4K4/6/7 kinases mediate ubiquitin signaling deficiency at low stiffness. Depletion of MAP4K4/6/7 kinases, but not MST1/2, resulted in a near-complete restoration of HR and NHEJ in cells at low stiffness (Fig. 3, K and L). The survival rate after irradiation was also restored in MM3KO cells at low stiffness (Fig. 3M). These data indicate that MAP4K4/6/7, but not MST1/2, mediate DNA repair inhibition by low stiffness.

We thus asked whether MAP4/6/7 regulate DNA repair through their downstream signaling LATS-YAP pathway. To test this, we
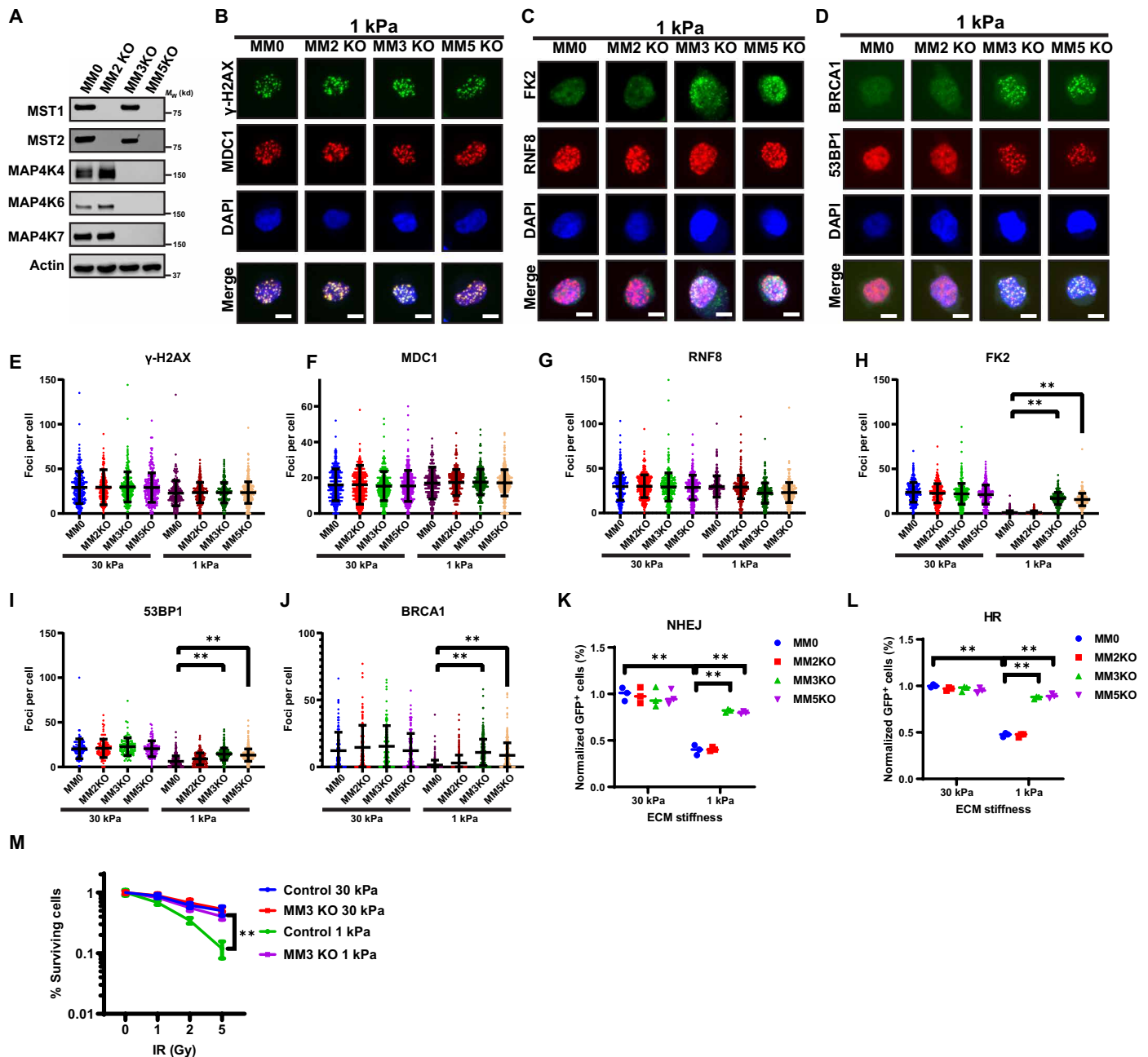
Fig. 3. Inhibition of DSB repair by low stiffness is dependent on MAP4K4/6/7. (**A**) Western blots showing the expression levels of MST1, MST2, MAP4K4, MAP4K6, and MAP4K7 in control (MM0), MM2KO, MM3KO, and MM5KO HEK293 cells. M_w, weight average molecular weight. (**B** to **D**) MM0, MM2KO, MM3KO, and MM5KO cells were grown on soft (1 kPa) and stiff (30 kPa) fibronectin-coated hydrogels. Cells were fixed 1 hour after irradiation (1 Gy) and stained with anti–γ-H2AX and MDC1 (B), RNF8 and FK2 (C), and 53BP1 and BRCA1 (D) antibodies. Scale bars, 10 μM. (**E** to **H**) Quantification of (B) to (D) is described in Methods. (**K** and **L**) MM0, MM2KO, MM3KO, and MM5KO cells were grown on soft (1 kPa) and stiff (30 kPa) fibronectin-coated hydrogels. Effect of ECM stiffness on the efficiency of NHEJ (K) and HR (L) in indicated cells was ana- lyzed by flow cytometry. (**M**) MAP4K4/6/7 kinases are required for regulation of stiffness-induced radiation sensitivity. Colony formation assays were performed to exam- ine survival of WT (MM0) and MM3KO HEK293 cells on soft (1 kPa) and stiff (30 kPa) fibronectin-coated hydrogels when exposed to the indicated doses of radiation.

used LATS1/2 knockout cells and YAP/TAZ knockout cells (fig. S5, A and B). As shown in fig. S5 (C to K), in LATS1/2 or YAP/TAZ knockout cells, low stiffness still blocked FK2/53BP1/BRCA1 foci formation. Furthermore, low stiffness also affected HR and NHEJ efficiency (fig. S5, L and M) and cellular sensitivity to IR (fig. S5N) in LATS1/2 knockout and YAP/TAZ knockout cells as in control cells.

These results suggest that the inhibition of DNA repair by MAP4K4/6/7 kinases at low stiffness is independent of LATS1/2-YAP.

MAP4K4/6/7 kinases phosphorylate ubiquitin at Thr[66]
The direct effect of MAP4K4/6/7 kinases on FK2 foci formation spurred us to test whether these kinases suppress RNF8 E3 ligase activity in a

fully recombinant system. Ubiquitination reactions were assembled with RNF8 in the presence or absence of MAP4K4/6/7 kinases. MAP4K4/6/7 kinases efficiently inhibited RNF8-mediated ubiquitin chain assembly (fig. S6, A and B), indicating that one or more of the components of the ubiquitin cascade might be phosphorylated by MAP4K4/6/7 kinases.

We next sought to determine substrates of MAP4K4/6/7 kinases in the ubiquitination reaction. In vitro kinase assays were performed with E1, E2, E3, or ubiquitin mixed with MAP4K4/6/7 kinases, and samples were subjected to phos-tag polyacrylamide gel electrophoresis (PAGE). No notable shift was found on E1, E2, or E3 using phos-tag gel (fig. S6, C to F), whereas one retarded mobility form of ubiquitin was specifically seen (Fig. 4A), indicating that mono ubiquitin itself is phosphorylated by MAP4K4 kinases. To determine the phosphorylation site, the phosphorylated ubiquitin was trypsinized and subjected to liquid chromatography tandem mass spectrometry (LC-MS/MS) analysis. One phosphorylated ubiquitin peptide 64 to 72 (ESpTLHLVLR) was identified (Fig. 4B), suggesting Thr^{66} phosphorylation. The phosphorylated ubiquitin can be specifically recognized by our homemade anti-pT66 antibody (Fig. 4C). Besides monomer Ub, we found that different ubiquitin chains can also be phosphorylated by MAP4K4 kinases in vitro (Fig. 4D). To confirm the phosphorylation site on ubiquitin, we mutated Thr^{66} on ubiquitin to alanine (T66A). Mutation of Thr^{66} prevented ubiquitin phosphorylation by MAP4K4 kinases (Fig. 4E).

We next checked whether phosphorylation of ubiquitin is regulated by ECM stiffness in cells. As shown in fig. S7A, low stiffness markedly induced phosphorylation of ubiquitin. Although the Hippo pathway can be regulated by multiple signals such as cell density, serum starvation, and energy stress, phosphorylation of ubiquitin was only slightly induced by these signals when compared to low stiffness condition (fig. S7A). We also found that the phosphorylation of ubiquitin was induced in multiple cell lines at low stiffness, indicating that this phosphorylation is a general event across different cell lines (fig. S7B). Furthermore, we found phosphorylated ubiquitin to be mainly localized in the nucleus, indicating that it might mainly regulate nuclear events (fig. S7C). To demonstrate the phosphorylation of Ub in cells, lysates from cells at low stiffness were trypsinized and subjected to LC-MS/MS analysis. Sixty-four to 72 pT66 were identified with high confidence, suggesting pT66 phosphorylation in cells (fig. S7D).

Since MAP4K4/6/7 kinases phosphorylated ubiquitin in vitro, we checked whether MAP4K4/6/7 regulate ubiquitin phosphorylation level in cells. Overexpression of MAP4K4/6/7 kinases increased the level of ubiquitin phosphorylation (Fig. 4F). Knockout MAP4/6/7 kinases decreased ubiquitin phosphorylation in cells at low stiffness, while knockout MST1/2 kinases had no notable effect (Fig. 4G). To test whether the kinase activity of MAP4K4/6/7 is required for ubiquitin phosphorylation, we reconstituted MAP4K4 wild-type (MAP4K4 WT) and kinase dead (MAP4K4 KD) mutant into MM3KO cell lines. As shown in Fig. 4H, phosphorylation of ubiquitin at low stiffness was restored in cells expressing MAP4K4 WT, but not in cells expressing MAP4K4 KD. Consistent with the upstream role of Rap2, knocking out Rap2 blocked ubiquitin phosphorylation in cells at low stiffness (Fig. 4I), However, knocking out LATS1/2 or YAP/TAZ had no notable effect on ubiquitin phosphorylation (Fig. 4J), indicating that Rap2-MAP4K4/6/7 pathway, but not LATS1/2-YAP signal, is required for low stiffness–induced ubiquitin phosphorylation.

Phosphorylation of ubiquitin blocks RNF8 mediated ubiquitin conjugation in vitro and in cells

We next examined the role of ubiquitin phosphorylation in RNF8-mediated ubiquitin chain assembly. We first examined whether phosphorylated ubiquitin affects RNF8-mediated ubiquitin chain assembly. We first purified phosphorylated ubiquitin via a biosynthesis system (37). With the purified phosphorylated ubiquitin (Fig. 5, A and B), we performed in vitro ubiquitination assays. The phosphorylated ubiquitin blocked ubiquitin chain assembly catalyzed by UbcH5C/RNF8 (Fig. 5C). RNF8 has been reported to work with several other E2s such as Ubc13, UBE2E1, UBE2E2, and UBE2E3 (38). We found that phosphorylation of ubiquitin blocked chain formation when different E2s were used together with RNF8 (Fig. 5D).

We next sought to determine the step in the ubiquitination reaction that is sensitive to phosphorylated ubiquitin. Not unexpectedly, phosphorylated ubiquitin was charged to E2 to a similar extent as nonphosphorylated ubiquitin (fig. S8A), indicating a similar efficiency of conjugation of E2. We thus hypothesized that phosphorylation of ubiquitin might affect RNF8 activity through disrupting the receptor function of ubiquitin. As shown in fig. S8B, discharging of UbcH5c ~ Ub by RNF8 was inhibited by phosphorylated ubiquitin. These results indicate that phosphorylation of ubiquitin inhibits RNF8-mediated UbcH5c discharging. Phosphorylated ubiquitin did not affect MDM2- or X-linked inhibitor of apoptosis (XIAP)–mediated ubiquitin chain assembly (extended data; fig. S8, C and D), indicating that the effect of phosphorylated ubiquitin might be limited to some specific E3 ligases and not the global ubiquitin system.

To study the role of ubiquitin phosphorylation in DNA repair regulation, we first used a phosphomimetic ubiquitin mutant T66E. The phosphomimetic ubiquitin mutant T66E totally blocked RNF8-mediated ubiquitin chain assembly (Fig. 5E), indicating that phosphomimetic ubiquitin has similar function as real phosphorylated ubiquitin. We thus generated cell lines stably expressing ubiquitin wild-type (WT), T66A, or T66E mutant and assessed their effect on the DSB repair pathway (Fig. 5F). We observed blocking effect of ubiquitin phosphorylation on histone H2A and H2Ax ubiquitination by T66E mutant (Fig. 5G). Furthermore, we also observed a drastic suppression of DNA damage–induced ubiquitin conjugation on chromatin (FK2 foci) and 53BP1 and BRCA1 foci formation in cells expressing T66E mutant (Fig. 5, H to P). These results strongly suggest that ubiquitin phosphorylation at Thr^{66} impairs the ubiquitin conjugation at DSB sites.

Phosphorylation of ubiquitin mediated DNA repair deficiency at low stiffness

To study the physiological function of Ub phosphorylation in cells at low stiffness, we used a Ub replacement strategy in HEK293 cells, wherein all endogenous copies of Ub were depleted by doxycycline (DOX)–inducible RNA interference while simultaneously expressing short hairpin RNA (shRNA)–resistant Ub WT and Ub T66A fused to the N terminus of ribosomal proteins L40 and S27a from a DOX-responsive promoter (fig. S9A) (39). Immunoblotting of extracts demonstrated similar levels of Ub WT, Ub T66A, and T66E proteins after DOX induction for 3 days (fig. S9B). In this Ub replacement system, low stiffness induced Ub phosphorylation only in cells expressing WT Ub, but not Ub T66A or Ub T66E (fig. S9C), further confirming that low stiffness leads to the phosphorylation of Ub at T66 in cells.
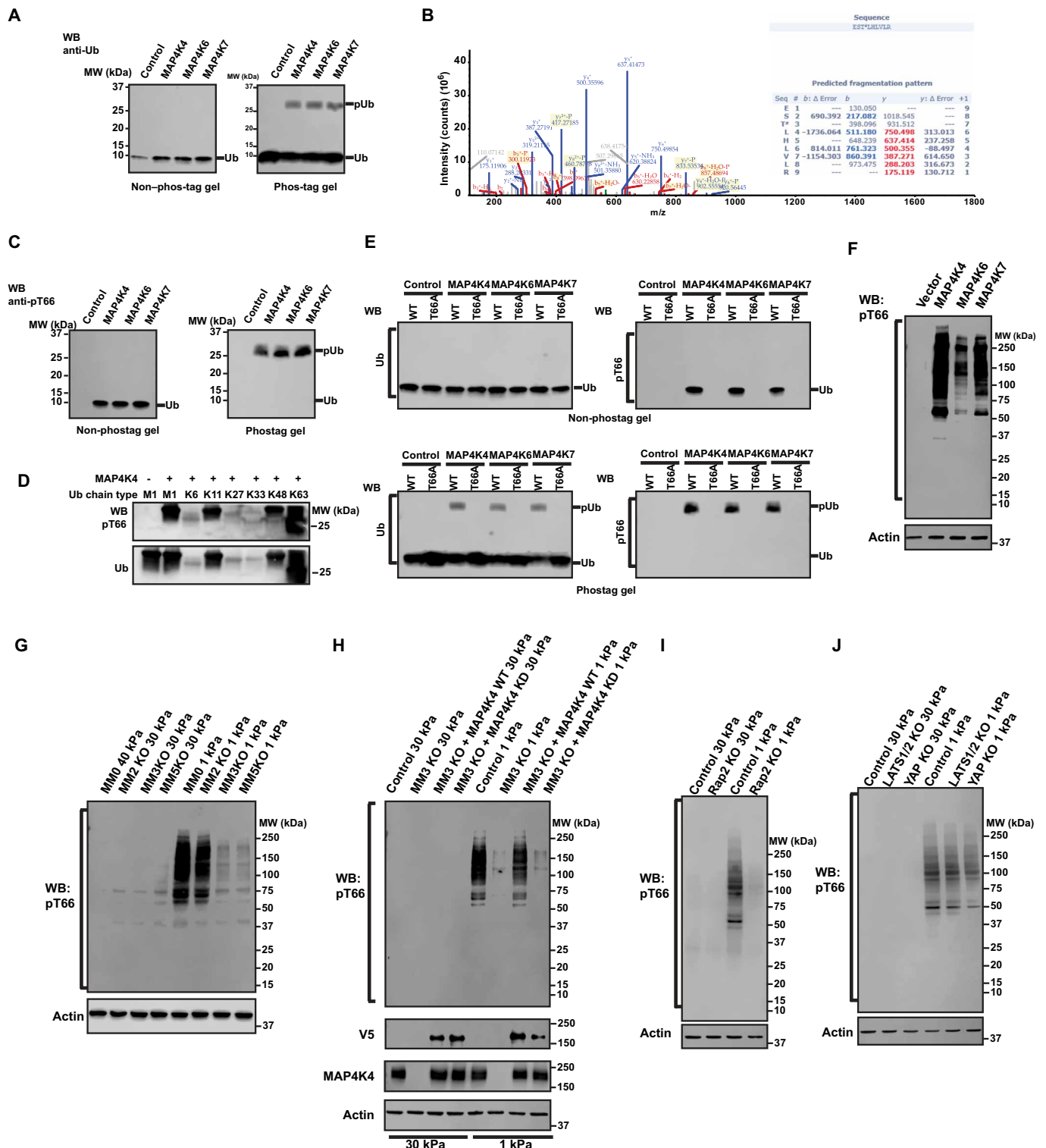
Fig. 4. MAP4K4/6/7 kinases phosphorylate ubiquitin in vitro and in cells. (**A**) An in vitro kinase assay was performed at 30°C for 1 hour in the presence of free Ub and indicated purified kinases. Samples were run on non–phos-tag or phos-tag PAGE and the gels were blotted with anti-Ub antibody. WB, Western blotting; MW, molecular weight. (**B**) Gel band of phosphorylated ubiquitin was trypsinized and subjected to LC-MS/MS analysis. (**C**) Samples were processed as in (A) and blotted with anti-pT66 antibody. (**D**) An in vitro kinase assay was performed with different tetra-Ub chains and MAP4K4. The gels were subjected to Western blot with anti-pT66 antibody (top) or anti-Ub antibody (bottom). (**E**) An in vitro kinase assay was performed with indicated Ub proteins and purified kinases. Samples were run on non–phos-tag or phos-tag PAGE, and the gels were blotted with anti-Ub or anti-pT66 antibody. WT, wild type. (**F**) HEK293 cells grown on plastic plates were transfected with the indicated constructs, and phosphorylation of ubiquitin in cells was detected with anti-pT66 antibody. Actin was used as a loading control. (**G** to **J**) Indicated cells were cultured on low (1 kPa) and high (30 kPa) stiffness fibronectin-coated hydrogels for 24 hours. Cell lysates were probed with indicated antibodies. Actin was used as loading control.
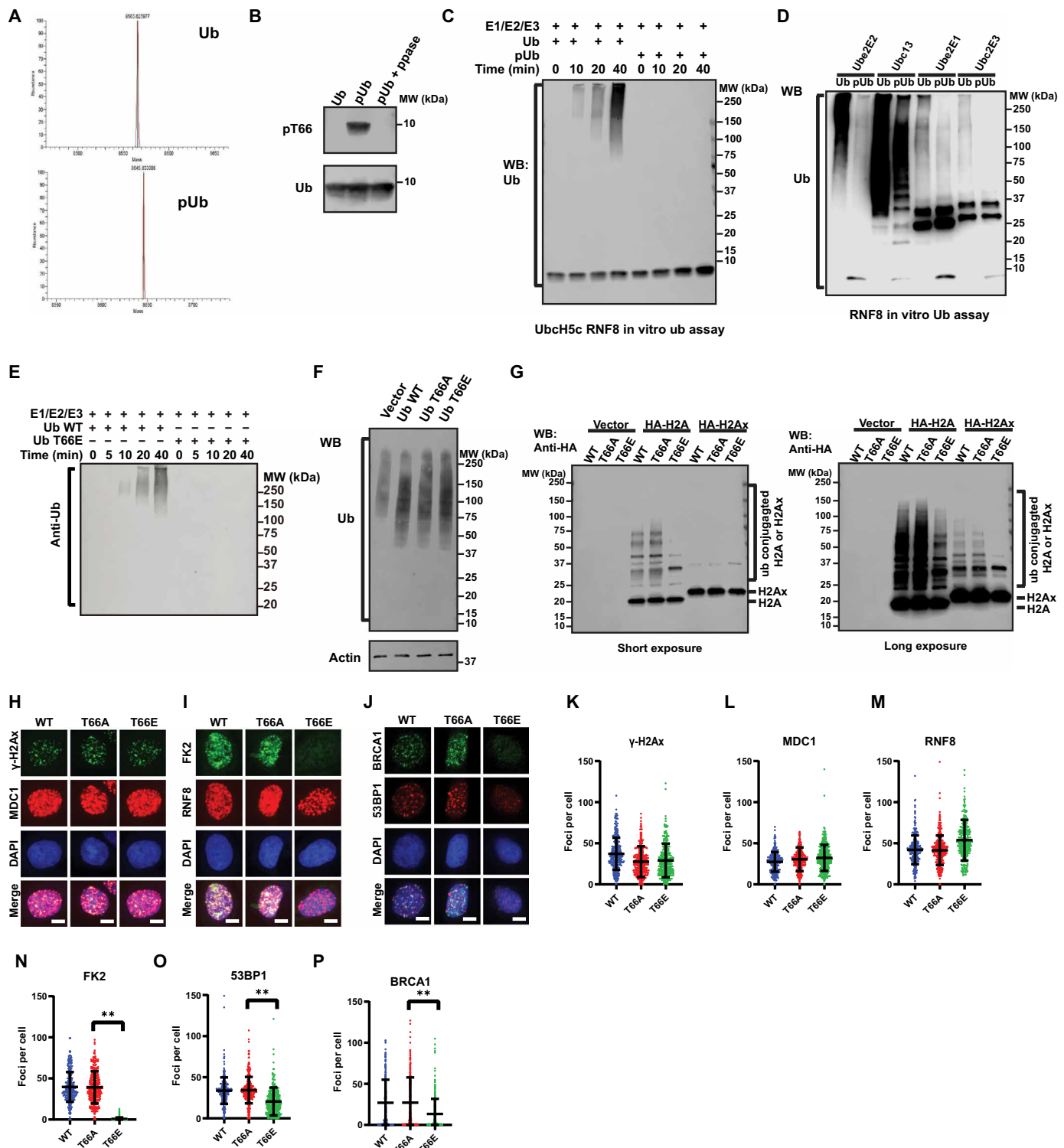
Fig. 5. Phosphorylation of ubiquitin blocks RNF8/RNF168–mediated ubiquitin conjugation in vitro and in cells. (**A**) Purified Ub variants were analyzed by electrospray ionization mass spectrometry. (**B**) Ub variants were treated with or without λ-PPase and blotted with indicated antibodies. (**C**) The assembly of ubiquitin chains was determined in the presence of Ube1, UbcH5c, and RNF8 and indicated Ub variants. Samples were taken at the indicated time and immunoblotted with anti-Ub antibody. (**D**) The assembly of ubiquitin chains was determined in the presence of Ube1, indicated E2s, RNF8, and indicated Ub variants. Polyubiquitin chains were detected by immunoblotting with an anti-Ub antibody. (**E**) The assembly of ubiquitin chains was determined in the presence of Ube1, UbcH5c, RNF8, and indicated Ub variants. Samples were taken at the indicated time and immunoblotted with anti-Ub antibody. (**F**) HEK293 expressing WT, T66A, and T66E mutant ubiquitin were blotted with anti-Ub antibody. (**G**) Cells as in (F) were transfected with indicated plasmids. Cells were irradiated (10 Gy) and blotted with anti-HA antibody. (**H** to **J**) Cells as in (F) were grown on glass cover slips. Cells were fixed 1 hour after irradiation (1 Gy) and stained with indicated antibodies. (**K** to **P**) Quantification of (H) to (J). **$P < 0.01$.
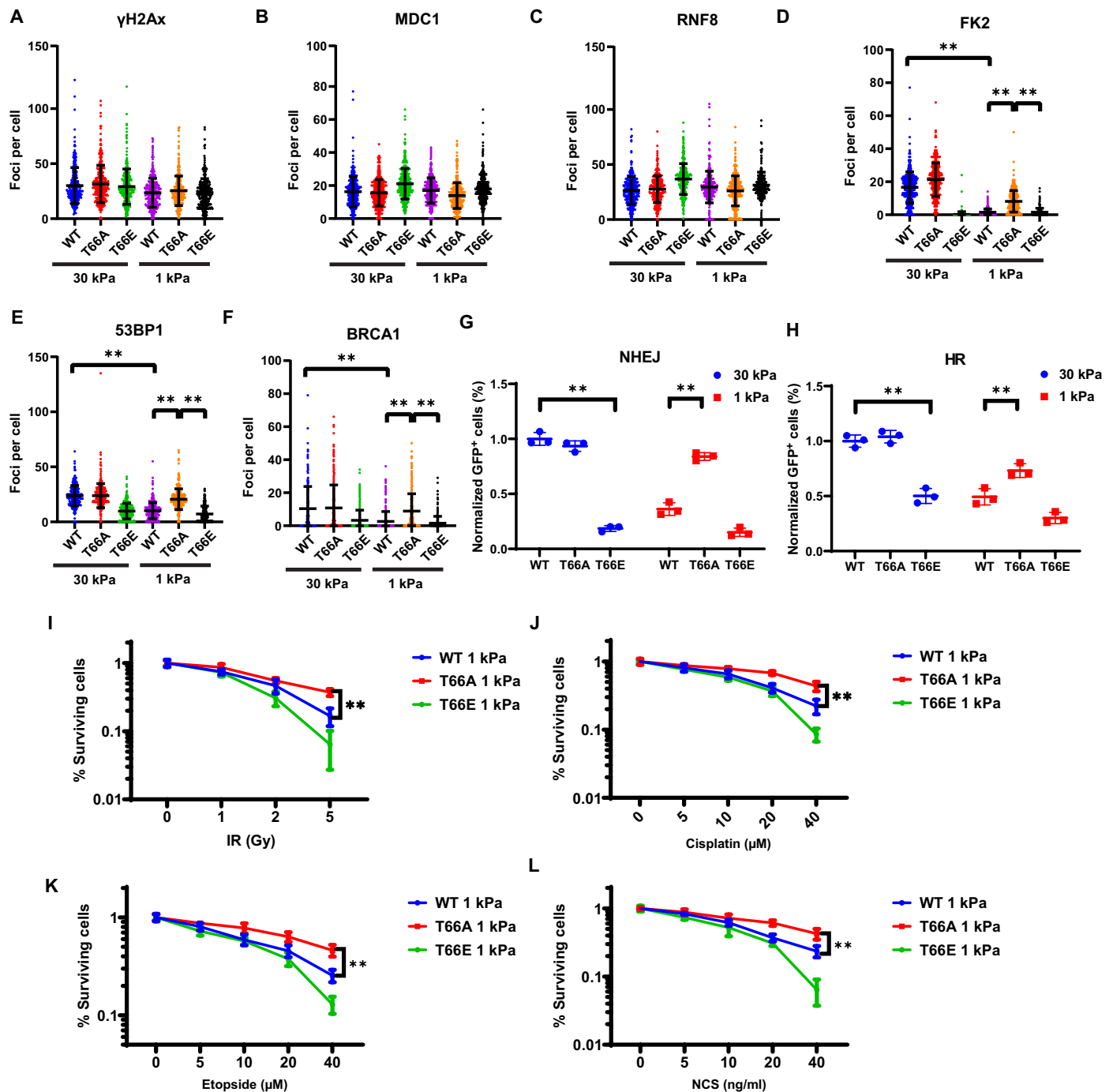
Fig. 6. Phosphorylation of ubiquitin mediated DNA repair blockage in cells at low stiffness. (**A** to **F**) Ubiquitin-replacement HEK293 cells expressing wild-type (WT), T66A, or T66E mutant ubiquitin were plated on soft (1 kPa) and stiff (30 kPa) fibronectin-coated hydrogels. Cells were fixed 1 hour after irradiation and stained with anti–γ-H2AX (A), MDC1 (B), RNF8 (C), FK2 (D), 53BP1 (E), and BRCA1 (F) antibodies. Data are presented as means ± SD, $n = 3$ biologically independent samples (**$P < 0.01$). (**G** and **H**) Phosphorylation of ubiquitin inhibits HR and NHEJ. Effect of ubiquitin phosphorylation on the efficiency of NHEJ (G) and HR (H) was analyzed by flow cytometry. Data are presented as means ± SD. $n = 3$ biologically independent samples (**$P < 0.01$). (**I** to **L**) Phosphorylation of ubiquitin regulates genotoxic sensitivity. Ubiquitin-replacement HEK293 cells expressing wild-type (WT), T66A, or T66E mutant ubiquitin were plated on soft (1 kPa) fibronectin-coated hydrogels. Cells were treated with indicated genotoxic agents. Colony formation assays were performed to examine survival of cells expressing wild-type (WT), T66A, or T66E mutant ubiquitin on soft (1 kPa) fibronectin-coated hydrogels. Data are presented as means ± SD. $n = 3$ biologically independent samples.

Low stiffness reduced FK2, 53BP1, and BRCA1 foci in ubiquitin replacement HEK293 cells expressing wild-type ubiquitin (Fig. 6, A to F, and fig. S9, D to F). However, low stiffness had little effect on FK2, 53BP1, and BRCA1 foci in ubiquitin replacement HEK293 cells expressing T66A mutant ubiquitin, suggesting that Ub-T66 phosphorylation is responsible for the impaired DSB repair under low stiffness. Notably, in ubiquitin replacement HEK293 cells expressing T66E mutant ubiquitin, FK2, 53BP1, and BRCA1 foci were blocked no matter whether the cells were cultured on stiff or soft hydrogel. These results indicated that phosphorylation of ubiquitin mediated DNA repair deficiency in cells at low stiffness condition. We further tested the effects of ubiquitin phosphorylation on HR and NHEJ. Both HR and NHEJ were inhibited in WT cells under low stiffness but were not affected in cells expressing ubiquitin T66A (Fig. 6, G and H). The lower survival rates in response to genotoxic agents were also reversed in cells expressing ubiquitin T66A at low stiffness (Fig. 6, I to L). Overall, we propose that MAP4K4/6/7-mediated phosphorylation of ubiquitin leads to DSB repair deficiency in cells at low stiffness conditions (fig. S9G).

DISCUSSION

Here, we conclude that cells limit DNA repair under low stiffness, which matches the proapoptosis status in soft tissue. This might represent an evolutionary strategy for cell to maintain genomic stability. Under low stiffness conditions, the Hippo-LATS pathway is activated (40), which promotes apoptosis and inhibits the prosurvival signaling. In the meanwhile, low stiffness also inhibits DNA repair pathway through Rap2-MAP4K4/6/7-ubiquitin signaling, which causes slow clearance of damaged DNA and further amplifies the proapoptotic signaling. These two effects together limit the expansion of genomically unstable cell populations by triggering their death.

ECM stiffness controls the HIPPO-YAP pathway to affect cell growth. As shown in fig. S5B, cell cycle was partially arrested at low stiffness. The percentage of G_1 cells increased around 8% from stiff to soft matrix. This change in cell cycle might contribute to decreased HR efficiency. However, we do not think that this 8% change would dominate the marked change of HR and NHEJ decrease in Fig. 1 L and M). To exclude the effect of HIPPO pathway and cell cycle, we further used LATS1/2 KO cells and TAZ/YAP KO cells to test the effect of ECM stiffness on HR and NHEJ. As shown in fig. S5B, the effect of stiffness on cell cycle was blocked in LATS1/2 KO cells and TAZ/YAP KO cells. However, in these cells, low stiffness also affected HR and NHEJ efficiency (fig. S5, L and M) and cellular sensitivity to IR (fig. S5N), indicating that ECM stiffness can regulate DNA repair independent of cell cycle effect.

We also noticed a slight decrease in γ-H2AX foci number at low stiffness (Fig. 2A). This indicated that the initial steps of DNA damage such as activation of ATM and meiotic recombination 11 homolog A (MRE11) might also be affected by ECM stiffness. However, this effect seems to be very mild. As shown in Fig. 2 (B and C), the slight change in γ-H2AX foci did not significantly affect the downstream effectors such as MDC1 and RNF8 recruitment. We thus mainly focused on the ubiquitination defect in our current study.

Ubiquitin signaling plays an important role in coordinating the recruitment of DSB repair factors such as BRCA1 and 53BP1. Extensive studies have identified components of the ubiquitin system that regulate ubiquitin signaling after DNA damage (8, 9, 13–17, 38).

Here, we showed that phosphorylation of ubiquitin at T66 blocked this ubiquitin signaling, providing a previously unknown layer of ubiquitin regulation in the DSB repair process. Further structural analysis will provide more detailed information on the mechanism regarding how this phosphorylation affects the RNF8-mediated ubiquitin system. Besides its role in DSB repair, ubiquitin is also involved in multiple cellular processes. Although phosphorylation of ubiquitin at T66 does not affect several E3 ubiquitin system such as MDM2 and XIAP (extended data; fig. S8, C and D), we could not exclude the possibility that phosphorylation of ubiquitin at T66 has additional effects within and outside of the DNA damage response (DDR) pathway.

In our current study, we found that ECM stiffness might be an important factor that regulates genotoxic sensitivity. Tumor stiffness thus might be used as a potential biomarker to predict chemotherapy and radiotherapy outcome. Furthermore, we found that the inhibition of DNA repair under low stiffness is dependent of MAP4K4/6/7 kinases. Given that the phosphorylation of ubiquitin is reversible, some phosphatase(s) in cells should be able to remove the phosphorylation of ubiquitin and promote DSB repair process. Pharmacological activating MAP4K4/6/7 kinases or inhibiting the potent phosphatase might promote ubiquitin phosphorylation and inhibit DSB repair, providing potential therapeutic strategies for the enhancement of the response to DSBs.

MATERIALS AND METHODS
Materials

Antibodies were obtained from the following sources: Ub (Santa Cruz Biotechnology, sc-8017), actin (Sigma-Aldrich, A2228), γ-H2AX (Millipore, 05-636), FLAG (Sigma-Aldrich, F1804), HA-tag [HA; Cell Signaling Technology (CST), 5017], Myc (Santa Cruz Biotechnology, 9E10), 53BP1 (Novus Biologicals, NB100-304), BRCA1 (Santa Cruz Biotechnology, sc-6954), FK2 (Millipore, 04-263), RNF8 (Novus Biologicals, H00009025-D01P, Anti-Ubiquitin Antibody), MAP4K4 (Bethyl, A301-503A), MAP4K6 (Novus, NBP1-22990), MAP4K7 (Genetex, GTX13141), YAP/TAZ (Santa Cruz Biotechnology, sc-101199), V5 (Abcam, ab9116), pLATS1 T1079 (CST, 8654), LATS1 (CST, 3477), LATS2 (CST,5888), MST1 (CST, 3682), MST2 (CST, 3952), and Rap2 (Biosciences, 610215). Fluorescein phalloidin were purchased from Invitrogen (F432). Phostag Acrylamide (304-93521/AAL-107) was purchased from Wako Chemicals. UBE1 (E1-304), UbcH5c (E2-627), UbcH6/UBE2E1 (E2–630), UbcH9/UBE2E3 (E2–678), UBE2N/UBE2V1 (Ubc13/Uev1a) complex (E2–664), Ub (U-100H), the Mdm2/HDM2 Ubiquitin Ligase Kit (K-200b), and the XIAP Ubiquitin Ligase Kit (K-250) were from R&D Systems. UBE2E2 were from Sigma-Aldrich (SRP6150-3NMOL). RNF8 and RNF168 proteins were purchased from Abnova. MST1, MST2, MAP4K4, MAP4K6, and MAP4K7 kinases were from SignalChem Inc. Neocarzinostatin (N9162), etoposide (E1383), and cisplatin (BP809) were from Millipore. Tetra-ubiquitin (Ub4) chains M1-linear, K6, K11, K29, K33, K48, and K63 were purchased from Boston Biochem.

Cell culture and transfection

HEK293, MCF-7, A549, U2OS, and MDA-MB-231 cell lines were purchased from American Type Culture Collection. The identities of all cell lines were confirmed by the Medical Genome facility at Mayo Clinic Center (Rochester, MN) using short tandem repeat

profiling upon receipt. Rap2 knockout (Rap2KO), MM2KO, MM3KO, MM5KO, LATS1/2 knockout (LATS1/2 KO), and YAP/TAZ knockout (YAP/TAZ KO) cells were generously provided by K. Guan (University of California San Diego, CA). The cell lines were maintained in Dulbecco's modified Eagle's medium (DMEM), McCoy's 5A, and RPMI 1640 with 10% fetal bovine serum, respectively. Plasmid transfections were performed using the transfection reagent Lipofectamine 2000 from Thermo Fisher Scientific Inc. For low confluence, 1.5×10^5 cells per well were seeded onto six-well plates. For high confluence, 8×10^5 cells were seeded per well. For all the other treatments, low confluence cells were treated with 2-deoxyglucose (25 mM), serum deprivation, and LatA (1 µg ml^{-1}).

Ub replacement system
HEK293 parental Ub-replacement cells were generated following previous protocol provided by Z. J. Chen (University of Texas Southwestern Medical Center, Dallas, TX). All Ub replacement cells were made as previously described (*25*).The HEK293 cell line stably expressing Ub shRNA and Ub WT, T66A, and T66E mutants was maintained in DMEM containing 10% tetracycline-free fetal bovine serum (Takara). DOX was added to the medium when indicated.

Plasmids
MAP4K4, MAP4K6, and MAP4K7 were cloned into pLEX_307 with a V5 tag. MAP4K4 kinase dead mutant K54R was generated by site-directed mutagenesis (StrataGene). pTO-sh Ub and pTO-Ub-WT plasmids were provided by Z. J. Chen (UT Southwestern). pTO-Ub-T66A and pTO-Ub-T66E was generated by site-directed mutagenesis (StrataGene). Plasmid encoding for His-tag USP2cc (pET15-USP2cc) was a gift from W. Harper (Harvard Medical school) and E. J. Bennett (University of California-San Diego). Wild-type Ub was cloned into pET-28a vector (Novagen). T66A and T66E were generated by site-directed mutagenesis (StrataGene).

Cell culture with polyacrylamide-based hydrogels for 2D and 3D culture
Hydrogels of different stiffness was made as described elsewhere (*41*), and elastic modulus were measured by atomic force microscopy (AFM). Human placenta fibronectin (10 µg/ml) were used to coat the sulfo-sanpah–activated hydrogels. Fibronectin-coating efficiency was measured as previous described (*42*). 3D culture followed a protocol described elsewhere (*35*).

Cell culture with Matrigel thick layer and Matrigel-coated plate
Plates were coated following manufacturer's guideline. Briefly, for Matrigel-coated coverslips, glass coverslips were incubated with 2% of Matrigel at room temperature for 1 hour. For thick layer gels, Matrigel (150 to 200 µl/cm^2) were coated onto glass coverslips.

Chromatin fractionation
Chromatin fractionation was performed largely as described previously but with several modifications (*43*). Cells were washed twice with ice-cold phosphate-buffered saline (PBS) and collected with an appropriate volume of ice-cold PBS followed by centrifugation at 1000*g* for 1 min. Cells were then preextracted with cytoskeletal (CSK) buffer containing 100 mM NaCl, 1× protease inhibitors (PI), 10 mM NaF, 20 mM *N*-ethylmaleimide, 0.25 mM phenylmethylsulfonyl fluoride (PMSF), and ribonuclease A (0.3 mg/ml) for 5 min

at room temperature. Chromatin fractions (pellet fraction) were prepared by centrifugation at 2000*g* for 5 min at 4°C and solubilized by sonication. Protein concentration of cell extracts was determined with Coomassie Protein Assay Reagent (Thermo Fisher Scientific).

Ubiquitin purification
Constructs of his$_6$-tagged Ub, Ub T66A, and T66E for bacterial expression were expressed in BL21 cells by inducing with 150 µM isopropyl-β-D-thiogalactopyranoside [IPTG; optical density at 600 nm (OD$_{600}$) ~ 1.0] at 18°C. The cells were grown at 18°C for 12 hours and lysed by sonication in His-Binding Buffer [50 mM tris-Cl (pH 8.0), 5 mM imidazole, 100 mM NaCl, 0.1 mM EDTA, and 1 mM PMSF]. After centrifugation (45,000*g*, 30 min, 4°C), the supernatant was applied to h Ni–nitrilotriacetic acid (NTA) agarose beads (Qiagen), agitated for 1 hour at 4°C, and subsequently washed in His-wash buffer [50 mM tris-Cl (pH 8.0), 300 mM NaCl, 10 to 20 mM imidazole, and 0.1 mM EDTA]. The his$_6$-tagged protein was eluted in His-elution buffer [50 mM tris-Cl (pH 8.0), 50 mM NaCl, 300 mM imidazole, and 0.1 mM EDTA]. Protein containing fractions were pooled, dialyzed to PBS, concentrated using a 3-kDa Molecular Weight Cutoff (MWCO) spin concentrator (Millipore), and flash-frozen in liquid nitrogen.

For purification of untagged ubiquitin, human ubiquitin DNA was subcloned into pET28a with N-terminal His$_6$-tag removed and C-terminal His$_6$-tag added through site-directed mutagenesis. Ubiquitin-6His-tag was transformed in Rossetta (DE3) *Escherichia coli* cells. A single colony was picked up and inoculated in Luria-Bertani medium (LB) for overnight incubation. A total of 10 ml overnight culture was diluted into 1 liter of fresh LB and grown until OD$_{600}$ = 0.4, and 1 mM IPTG was added. Cells were further incubated at 16°C for 16 hours. Cells were pelleted and purified by Ni-NTA beads followed by removal of the C-terminal fusion protein by incubation overnight with His-USP2cc. His-USP2cc and C-terminal fusion protein were removed by Ni-NTA binding.

For purification of phosphorylated ubiquitin, BL21 (DE3) ΔserC cells were cotransformed with pNHD_Ub66TAG and pUC_pThrRS_SeptRNAv2.0CUA_OXB20-PduX_EFSep. A single colony was picked up and inoculated in LB for overnight incubation. A total of 20-ml overnight culture was diluted into 1 liter of fresh LB and grown until OD$_{600}$ = 0.6, and 1 mM IPTG was added. Cells were further incubated at 37°C for 6 hours and pelleted before purification as described above.

Validation of purified phosphorylated ubiquitin by mass spectrometry
Both Ub and pUb were dialyzed to H$_2$O. Protein samples were loaded via U-pick up injection mode onto an Agilent Zorbax 300SB-C3 5 µm 150 mm by 0.5 mm column. The Dionex Ultimate 3000 ultra-high-performance liquid chromatography (UHPLC) system (NCS-3500RS pump and WPS-3000PL autosampler) was used for reverse phase chromatography where solvent A was 100% H$_2$O and 0.1% formic acid (FA), and solvent B was 100% acetonitrile (ACN) and 0.1% FA. High-performance liquid chromatography was run in the capillary flow mode with a flow rate of 12 µl/min. A 25-min linear gradient was used (0 to 2 min, 10% B; ramped to 90% B in 13 min, held at 90% B for 5 min, ramped back to 10% B in 1 min, and last held at 10% B for 4 min). The coupled Thermo LTQ-XL ion trap mass spectrometer was operated in a scanning mode using Xcalibur v2.6 software. The global parameters were as follows: ion source, ESI; ionization mode, positive; spray voltage, 5000 V; ion transfer

tube temperature, 275°C; sheath gas 8, auxiliary gas 1; tube lens, 135 V; automatic gain control (AGC) target was 3×10^4; maximum injection time was 10 ms; data type was profile; and scan range was 500 to 200 mass/charge ratio (m/z). Raw files were loaded into and processed by software Protein Deconvolution (Thermo).

In vitro ubiquitination assay
Briefly, E1 (60 nM), indicated E2s (200 nM), and RNF8 (300 nM) or RNF168 (300 nM) were incubated with ubiquitin (10 μM) at 30°C in buffers containing 25 mM tris HCl (pH 7.4), 2 mM adenosine 5′-triphosphate (ATP), 5 mM MgCl₂, 5 mM MnCl₂, and 0.1 mM dithiothreitol (DTT). Protein kinases (100 ng) were included in a 50-μl reaction as indicated to test their effect on ubiquitination.

In vitro kinase assay
Purified protein kinases (100 ng) were incubated with 1 μg of E1, E2, E3, or ubiquitin in the kinase reaction buffer [15 mM Hepes (pH 7.0), 1 mM dithiothreitol, 5 mM MgCl₂, 5 mM MnCl₂, and 1 mM ATP] at 30°C for 30 min. The product was separated by SDS-PAGE or phos-tag PAGE.

E2 charging assays
Phosphorylated ubiquitin or nonphosphorylated ubiquitin (40 μM) was incubated with 4 μM UbcH5c, 0.1 μM E1, and 2 mM Mg-ATP for indicated time. The reaction was stopped with sample buffer without DTT. The samples were resolved on SDS-PAGE, and gel was stained with Coomassie Brilliant Blue.

E2 discharge assays
Ubc5Hc charged with Ub (5 μg) was mixed with ub-His6 or phos-Ub-His6 with RNF8 or buffer as control in buffer 50 mM tris/HCl (pH 7.5), 100 mM NaCl, 10 mM MgCl₂, 1 μM ZnCl₂, and 1 mM tris (2-carboxyethyl) phosphine (TCEP). Samples were stopped at given times and were analyzed by SDS-PAGE.

Identification of phosphorylation sites on ubiquitin after in vitro kinase assay
Ubiquitin was phosphorylated by MAP4K4 in vitro and run on phos-tag gel. The phosphorylated ubiquitin bands were cut, and in-gel trypsin digestion was carried out as described (44) with modifications. After the gels were extensively washed with water, gels were excised, diced into 2×2 mm cubes, and destained by 1 ml of 50 mM ammonium bicarbonate (AMBC)/50% ACN with agitation for 1 hour; then, the gels were further washed by 1 ml of 50 mM AMBC/50% ACN for three times. Last, 100% ACN wash was performed to ensure complete gel dehydration. Trypsin solution (20 ng/μl) was prepared on ice using prechilled 50 mM AMBC (pH 8.0). Trypsin solution was subsequently added to gel pieces at approximately equivalent volume and incubated on ice for 30 min. Another 1× gel volume of trypsin solution was added to gel samples and incubated an additional 1 hour on ice for a total incubation time of 1.5 hour before transferring samples to 37°C for overnight digestion. Digests were quenched and extracted by addition of 50 μl of 50% ACN/0.3% FA for 1 hour by shaking. The digested peptides were recovered into fresh Protein LoBind tubes, and additional extraction step was performed with 80% ACN/0.3% FA for 30 min. The extracted peptides were combined and dried in a SpeedVac.

Samples were loaded via user-defined program onto a home-packed 75 um × 200-mm Luna C18 column (Emitter from New

Objective, Woburn, MA; Luna C18 particles from Phenomenex, Torrance, CA). The Dionex Ultimate 3000 UHPLC System (NCS-3500RS pump and WPS-3000PL autosampler) was used for reverse phase chromatography where solvent A was 100% H2O and 0.1% FA, and solvent B was 100% ACN and 0.1% FA. A 40-min linear gradient was used (0 min, 2% B, flow rate of 1 μl/min; 5 min, 2% B, flow rate of 1 μl/min; 5.5 min, 2% B, flow rate of 0.3 μl/min; 7 min, 7% B, flow rate of 0.3 μl/min; 30 min, 30% B, flow rate of 0.3 μl/min; 31 min, 90% B, flow rate of 1 μl/min; 35 min, 90% B, 1 μl/min; 36 min, 2% B, flow rate of 1 μl/min; 40 min, 2% B, flow rate of 1 μl/min). The coupled Thermo Fusion Lumos mass spectrometer was operated in both data-dependent and targeted MS/MS mode, using Xcalibur v4.2 software. The global parameters were as follows: ion source, NSI; ionization mode, positive; spray voltage, 2100 V; ion transfer tube temperature, 275°C; no sheath gas or auxiliary gas was used. For data-dependent mode, (i) mass spectrometry (MS1) resolution was 60,000, scan range was 300 to 1800 mz, radio frequency (RF) lens (%) of 60, AGC target of 4.0×10^5, maximum injection time of 50 ms, intensity threshold of 5.0×10^4, and dynamic exclusion of 15 s; (ii) isolation mode quadrupole, isolation window of 2 m/z, higher collisional dissociation (HCD) collision energy of 35, orbitrap resolution of 7500, AGC target of 1.0×10^5, and maximum injection time of 100 ms. For targeted MS/MS mode, the isolation window was 1.6 m/z, isolation mode was quadrupole, detector was orbitrap, activation type was HCD with a collision energy of 35%, orbitrap resolution was 30,000; scan range was 300 to 1800 m/z, AGC target was 1×10^5, and maximum injection time was 50 ms. Raw files were searched against human ubiquitin protein sequence for phosphorylation site in Proteome Discoverer 2.1 (Thermo Fisher Scientific).

Antibody generation
Antigen peptide (NIQKESpTLHLVLRC) was synthesized by Peptide 2.0 and was conjugated with keyhole limpet hemocyanin as immunogen, and rabbits were immunized with the conjugated peptide. The antisera were affinity-purified with AminoLink Plus immobilization and purification kit (Pierce).

Phos-tag PAGE assay
To detect phosphorylated proteins using SDS-PAGE, 12% polyacrylamide gels containing 25 μM phos-tag acrylamide (Wako chemicals) and 50 μM MnCl₂ were used. After electrophoresis, phos-tag acrylamide gels were washed with gentle shaking in transfer buffer containing 0.01% SDS and 1 mM EDTA for 10 min and then incubated in transfer buffer containing 0.01% SDS without EDTA for 10 min according to the manufacturer's protocol. Proteins were transferred to polyvinylidene difluoride membranes and studied by conventional immunoblot analysis.

Immunoblotting and immunoprecipitation
We prepared cell lysates and performed immunoprecipitation and immunoblotting as previously described (45). Briefly, cells were lysed with NETN buffer [20 mM tris-HCl (pH 8.0), 100 mM NaCl, 1 mM EDTA, and 0.5% Nonidet P-40] containing 50 mM β-glycerophosphate, 10 mM NaF, and pepstatin A and aprotinin (1 mg/ml each). Whole-cell lysates were centrifuged at 12,000 rpm for 15 min. Whole-cell lysates were incubated with 2 μg of antibody and protein A or protein G Sepharose beads (Amersham Biosciences) for 2 hours or overnight at 4°C. The immunocomplexes were then washed with

NETN buffer three times and separated by SDS-PAGE. Immuno-blotting was performed following standard procedures.

Immunofluorescence

To visualize IR-induced foci, cells were cultured on coverslips and treated with 1-gray (Gy) irradiation followed by recovery for 1 hour. Cells were then washed in PBS, fixed with 3% paraformaldehyde for 15 min, and permeabilized in 0.5% Triton solution for 30 mins at room temperature. Samples were blocked with 5% goat serum and then incubated with primary antibody at 4° overnight. Samples were washed three times and incubated with secondary antibody at 37° for 30 min. Cells were stained with 4′,6-diamidino-2-phenylindole (DAPI) to visualize nuclear DNA. The coverslips were mounted onto glass slides with anti-fade solution.

Image acquisition was controlled by MetaXpress software (Molecular Devices). The cell layer was detected by an autofocus. To cover the whole nucleus, we acquired 30 z sections with a step size of 0.2 μm around the autofocus position. Z-stacks images were projected and analyzed using the Custom Module Editor function of the MetaXpress software (Molecular Devices, V6.2). For detection of nuclei, a nuclear mask was created using the DAPI staining and appropriate settings for nuclear area, perimeter, and intensities. The nuclear mask was then used to measure several intensity-based features for all readouts and to measure properties of DNA damage–induced foci within nuclei. Foci detection was performed using morphological top-hat filtering followed by threshold-based segmentation of objects. Single cell–based values were exported to Excel spreadsheets for data analysis.

Colony formation assay

Hydrogels of different stiffness on coverslip were placed in six-well plate, and 500 to 5000 cells were plated in triplicate in each well of six-well plates. Sixteen hours later, cells were exposed to IR or treated with indicated chemotherapy drugs and incubated for 10 to 14 days at 37°C to allow colony formation. Colonies were stained with methylene blue and were counted. Results were normalized to plating efficiencies.

Apoptosis analysis

Adherent cells were trypsinized into single cells and were rinsed with warm PBS. The fluorescein isothiocyanate (FITC)–Annexin V Apoptosis Detection Kit (BD Bioscience) was used according to the manufacturer's protocol. Briefly, floating cells were resuspended in binding buffer at a final density of 10^6 cells/ml. FITC-annexin (5 μl) and PI (5 μl) were added to 100 μl of the cell suspension containing 10^5 cells. The cell suspension was mixed by gently vortexing and then incubated for 15 min at room temperature in the dark. Subsequently, 400 μl of binding buffer was added, and cells were analyzed by flow cytometry using Attune NxT Flow Cytometer (Thermo Fisher Scientific).

DNA repair assays and fluorescence-activated cell sorting analysis

Cells expressing DR-GFP (for HR) or pEGFP-Pem1-Ad2 (for NHEJ) were seeded at 5×10^5 cells per 10-cm dish and were cultured for 48 hours. The cells then were transfected with 5 μg of I–Sce I (to induce DSBs), 15 ng of mCherry (as an internal reference to monitor transfection efficiency), and the indicated plasmids. Eight hours after transfection, cells were trypsinized and plated on low- or high-

stiff ECM. DSB repair efficiency was analyzed by fluorescence-activated cell sorting on an Attune NxT Flow Cytometer (Thermo Fisher Scientific). The efficiency of homologous recombination or of NHEJ was ascertained as the ratio of GFP$^+$ cells and DsRed$^+$ cells, respectively. At least 20,000 cells were counted. Experiments were performed in triplicate.

Neutral comet assays

The Comet Assay Single-Cell Gel Electrophoresis Assay Kit (Trevigen) was used according to the manufacturer's protocol. Briefly, cells were irradiated with or without 10 Gy of IR and recovered for indicated time at 37°C. Cells were collected and rinsed twice with ice-cold PBS; 1×10^5/ml cells were combined with 1% low melting (LM) Agarose at 37°C at the ratio of 1:10 (v/v) and immediately pipetted onto slides. For cellular lysis, the slides were immersed in the lysis buffer overnight at 4°C. Then, the slides were subjected to electrophoresis at 21 V for 45 min and stained in SYBR for 20 min. All images were taken with a fluorescence microscope and analyzed by ImageJ with OpenComet.

Preparation of semisynthetic hyaluronan-derived hydrogels

Under aseptic conditions, Glycosil (ESI Bio, GS222), Gelin-S, (ESI Bio, GS231), and Extralink (ESI Bio, GS3006) were dissolved in degassed water (ESI Bio, GS240) according to the manufacturer's directions. To make soft hydrogels, stock concentrations of Glycosil (10 mg/ml), Gelin-S (10 mg/ml), and Extralink (5 mg/ml) were made as per the manufacturer's directions. To make stiff hydrogels, concentrated stocks of Glycosil and Extralink were prepared by solubilization in reduced volumes to make 2× Glycosil and 5× Extralink. Before use, aliquots were taken from each vial to make solutions at 1:5 ratios of Extralink (Glycosil + Gelin-S) and 5× Extralink (2× Glycosil + Gelin-S) for soft and stiff hydrogels, respectively. For all conditions, the amount of Gelin-S was kept constant to ensure the same number of gelatin-based cell binding sites.

In vivo mice study using LOX inhibitor BAPN

All animal experiments were performed in accordance with a protocol approved by the Institutional Animal Care and Use Committee of Mayo clinic. Mouse mammary tumor 4 T1 cells (1×10^6) were injected into the mammary gland of Balb/c mice. Two weeks after injection (tumor size around 100 mm^3), mice were intraperitoneally injected with cisplatin at a dose of body weight (6 mg/kg) twice per week with or without BAPN (3 mg/kg; Spectrum) administered in drinking water. Tumor growth was measured using a Vernier caliper at the indicated times after injection, and the tumor volume was calculated as length × width × height/2. Four weeks later, mice were euthanized, and tumors were removed and weighed.

In vivo mice study using hydrogel

MDA-MB-231 cells (5×10^6) in 20 μl PBS suspensions were embedded into 200 μl of soft and stiff formulations as described in the preparation of hydrogels. After brief gelation (5 min) at room temperature, the cell-laden hydrogels were subcutaneously injected into athymic nude mice. Mice were intraperitoneally injected with cisplatin at a dose of body weight (1 mg/kg) twice per week. Tumor growth was measured using a Vernier caliper at the indicated times after injection, and the tumor volume was calculated as length × width × height/2. Five weeks later, mice were euthanized, and tumors were removed and weighed.

AFM measurements

The stiffness of hydrogel was estimated using Bioscope Catalyst Atomic Force Microscope (Bruker) with a 2.5-μm radius, sphere-tipped AFM tip (Novascan). The spring constant of the AFM tip was determined at ~120 pN/nm by thermal fluctuation method (46). Hydrogel samples were submersed in PBS and indented at low indentation rate (0.5 Hz) with a trigger force of 5 nN. Twenty-five force curves were performed over a 100 μm by 100 μm area (grid of 5 × 5 points separated by 20-μm distance) using MIRO 2.0 (Nano-Scope 9.1; Bruker). The elastic modulus (Young's modulus) E was then extracted from each force curve by the fitting (NanoScope Analysis software, v1.8, Bruker) with the Hertz contact model for spherical indenter and following the relationship (Eq. 1)

$$E = \frac{3}{4} \frac{(1 - \nu^2)}{R^{1/2} \delta^{3/2}} F \tag{1}$$

with R as the tip radius, ν the Poisson's ratio defined at 0.45 for hydrated hydrogels, and δ as the sample indentation. In total, two areas per hydrogel sample were analyzed, and two samples were prepared per hydrogel stiffness value ($n = 3$).

Detection of ubiquitin phosphorylation in cells by MS

HEK293 cells were plated on 30 and 1 kPa hydrogel for 24 hours. Cells were washed twice with ice-cold PBS and harvested in 10 mM tris-HCl (pH 7.5), 10 mM KCl, 1.5 mM MgCl2, 10 mM glycerol 2-phosphate, 50 mM sodium fluoride, 5 mM sodium pyrophosphate, 0.5 mM EGTA, 1 mM sodium orthovanadate, 5 mM TCEP, 1 mM PMSF, aprotinin (1 μg/ml), leupeptin (1 μg/ml), and phosphatase inhibitor cocktail. Cell lysates were loading on SDS-PAGE. The whole lane was cut, and in-gel trypsin digestion was carried out as described (44) with modifications. After the gels were extensively washed with water, gels were excised, diced into 2×2 mm cubes, and destained by 1 ml of 50 mM AMBC/50% ACN with agitation for 1 hour; then, the gels were further washed by 1 ml of 50 mM AMBC/50% ACN for three times. Last, 100% ACN wash was performed to ensure complete gel dehydration. Trypsin solution (20 ng/μl) was prepared on ice using prechilled 50 mM AMBC (pH 8.0). Trypsin solution was subsequently added to gel pieces at approximately equivalent volume and incubated on ice for 30 min. Another 1× gel volume of trypsin solution was added to gel samples and incubated an additional 1 hour on ice for a total incubation time of 1.5 hours before transferring samples to 37°C for overnight digestion. Digests were quenched and extracted by addition of 50 μl of 50% ACN/0.3% FA for 1 hour by shaking. The digested peptides were recovered into fresh Protein LoBind tubes, and additional extraction step was performed with 80% ACN/0.3% FA for 30 min. The extracted peptides were combined and dried in a SpeedVac.

Samples were processed for MS and analyzed as described above (see the section, "Validation of purified phosphorylated ubiquitin").

Statistical analyses

Statistical analysis was used to support the main conclusions in this study. Unless otherwise specified, all experiments were performed at least three times. The sample size for each experiment is provided in the relevant figure legends and/or earlier and, unless otherwise specified, represents biological replicates or independent experiments performed on different days, each with technical triplicates. All values are reported as means ± SEM or SD as indicated. Statistical signifi-cance for all pairwise comparisons was evaluated with a two-tailed Student's t test or two-way analysis of variance (ANOVA) test, a P value of <0.05 was considered significant, and $P < 0.01$ was consid-ered very significant. To our knowledge and observation, all of the biochemical measurements made provided data that is of a normal distribution, and there is a similar variance among the groups.

REFERENCE AND NOTES

1. H. C. Reinhardt, M. B. Yaffe, Phospho-Ser/Thr-binding domains: Navigating the cell cycle and DNA damage response. Nat. Rev. Mol. Cell Biol. 14, 563–580 (2013).
2. C. H. Bassing, K. F. Chua, J. Sekiguchi, H. Suh, S. R. Whitlow, J. C. Fleming, B. C. Monroe, D. N. Ciccone, C. Yan, K. Vlasakova, D. M. Livingston, D. O. Ferguson, R. Scully, F. W. Alt, Increased ionizing radiation sensitivity and genomic instability in the absence of histone H2AX. Proc. Natl. Acad. Sci. U.S.A. 99, 8173–8178 (2002).
3. A. Celeste, S. Petersen, P. J. Romanienko, O. Fernandez-Capetillo, H. T. Chen, O. A. Sedelnikova, B. Reina-San-Martin, V. Coppola, E. Meffre, M. J. Difilippantonio, C. Redon, D. R. Pilch, A. Olaru, M. Eckhaus, R. D. Camerini-Otero, L. Tessarollo, F. Livak, K. Manova, W. M. Bonner, M. C. Nussenzweig, A. Nussenzweig, Genomic instability in mice lacking histone H2AX. Science 296, 922–927 (2002).
4. E. P. Rogakou, D. R. Pilch, A. H. Orr, V. S. Ivanova, W. M. Bonner, DNA double-stranded breaks induce histone H2AX phosphorylation on serine 139. J. Biol. Chem. 273, 5858–5868 (1998).
5. G. S. Stewart, B. Wang, C. R. Bignell, A. M. R. Taylor, S. J. Elledge, MDC1 is a mediator of the mammalian DNA damage checkpoint. Nature 421, 961–966 (2003).
6. M. Goldberg, M. Stucki, J. Falck, D. D'Amours, D. Rahman, D. Pappin, J. Bartek, S. P. Jackson, MDC1 is required for the intra-S-phase DNA damage checkpoint. Nature 421, 952–956 (2003).
7. Z. Lou, K. Minter-Dykhouse, X. Wu, J. Chen, MDC1 is coupled to activated CHK2 in mammalian DNA damage response pathways. Nature 421, 957–961 (2003).
8. C. Doil, N. Mailand, S. Bekker-Jensen, P. Menard, D. H. Larsen, R. Pepperkok, J. Ellenberg, S. Panier, D. Durocher, J. Bartek, J. Lukas, C. Lukas, RNF168 binds and amplifies ubiquitin conjugates on damaged chromosomes to allow accumulation of repair proteins. Cell 136, 435–446 (2009).
9. G. S. Stewart, S. Panier, K. Townsend, A. K. al-Hakim, N. K. Kolas, E. S. Miller, S. Nakada, J. Ylanko, S. Olivarius, M. Mendez, C. Oldreive, J. Wildenhain, A. Tagliaferro, L. Pelletier, N. Taubenheim, A. Durandy, P. J. Byrd, T. Stankovic, A. M. R. Taylor, D. Durocher, The RIDDLE syndrome protein mediates a ubiquitin-dependent signaling cascade at sites of DNA damage. Cell 136, 420–434 (2009).
10. M. S. Y. Huen, R. Grant, I. Manke, K. Minn, X. Yu, M. B. Yaffe, J. Chen, RNF8 transduces the DNA-damage signal via histone ubiquitylation and checkpoint protein assembly. Cell 131, 901–914 (2007).
11. N. K. Kolas, J. R. Chapman, S. Nakada, J. Ylanko, R. Chahwan, F. D. Sweeney, S. Panier, M. Mendez, J. Wildenhain, T. M. Thomson, L. Pelletier, S. P. Jackson, D. Durocher, Orchestration of the DNA-damage response by the RNF8 ubiquitin ligase. Science 318, 1637–1640 (2007).
12. N. Mailand, S. Bekker-Jensen, H. Faustrup, F. Melander, J. Bartek, C. Lukas, J. Lukas, RNF8 ubiquitylates histones at DNA double-strand breaks and promotes assembly of repair proteins. Cell 131, 887–900 (2007).
13. S. Panier, D. Durocher, Regulatory ubiquitylation in response to DNA double-strand breaks. DNA Repair 8, 436–443 (2009).
14. H. Kim, J. Chen, X. Yu, Ubiquitin-binding protein RAP80 mediates BRCA1-dependent DNA damage response. Science 316, 1202–1205 (2007).
15. B. Sobhian, G. Shao, D. R. Lilli, A. C. Culhane, L. A. Moreau, B. Xia, D. M. Livingston, R. A. Greenberg, RAP80 targets BRCA1 to specific ubiquitin structures at DNA damage sites. Science 316, 1198–1202 (2007).
16. B. Wang, S. Matsuoka, P. B. Carpenter, S. J. Elledge, 53BP1, a mediator of the DNA damage checkpoint. Science 298, 1435–1438 (2002).
17. J. Yan, Y.-S. Kim, X.-P. Yang, L.-P. Li, G. Liao, F. Xia, A. M. Jetten, The ubiquitin-interacting motif–containing protein RAP80 interacts with BRCA1 and functions in DNA damage repair response. Cancer Res. 67, 6647–6656 (2007).
18. J. D. Humphrey, E. R. Dufresne, M. A. Schwartz, Mechanotransduction and extracellular matrix homeostasis. Nat. Rev. Mol. Cell Biol. 15, 802–812 (2014).
19. J. Li, Z. Zhao, J. Wang, G. Chen, J. Yang, S. Luo, The role of extracellular matrix, integrins, and cytoskeleton in mechanotransduction of centrifugal loading. Mol. Cell. Biochem. 309, 41–48 (2008).

20. M. A. Schwartz, Integrins and extracellular matrix in mechanotransduction. *Cold Spring Harb. Perspect. Biol.* **2**, a005066 (2010).

21. Z. Meng, Y. Qiu, K. C. Lin, A. Kumar, J. K. Placone, C. Fang, K.-C. Wang, S. Lu, M. Pan, A. W. Hong, T. Moroishi, M. Luo, S. W. Plouffe, Y. Diao, Z. Ye, H. W. Park, X. Wang, F.-X. Yu, S. Chien, C.-Y. Wang, B. Ren, A. J. Engler, K.-L. Guan, RAP2 mediates mechanoresponses of the Hippo pathway. *Nature* **560**, 655–660 (2018).

22. Z. Meng, T. Moroishi, V. Mottier-Pavie, S. W. Plouffe, C. G. Hansen, A. W. Hong, H. W. Park, J.-S. Mo, W. Lu, S. Lu, F. Flores, F.-X. Yu, G. Halder, K.-L. Guan, MAP4K family kinases act in parallel to MST1/2 to activate LATS1/2 in the Hippo pathway. *Nat. Commun.* **6**, 8357 (2015).

23. A. J. Engler, S. Sen, H. L. Sweeney, D. E. Discher, Matrix elasticity directs stem cell lineage specification. *Cell* **126**, 677–689 (2006).

24. S. Dupont, L. Morsut, M. Aragona, E. Enzo, S. Giulitti, M. Cordenonsi, F. Zanconato, J. Le Digabel, M. Forcato, S. Bicciato, N. Elvassore, S. Piccolo, Role of YAP/TAZ in mechanotransduction. *Nature* **474**, 179–183 (2011).

25. F. A. Venning, L. Wullkopf, J. T. Erler, Targeting ECM disrupts cancer progression. *Front. Oncol.* **5**, 224 (2015).

26. M. C. Lampi, C. A. Reinhart-King, Targeting extracellular matrix stiffness to attenuate disease: From molecular mechanisms to clinical trials. *Sci. Transl. Med.* **10**, eaao0475 (2018).

27. N. P. Talele, J. Fradette, J. E. Davies, A. Kapus, B. Hinz, Expression of α-smooth muscle actin determines the fate of mesenchymal stromal cells. *Stem Cell Reports* **4**, 1016–1030 (2015).

28. H. A. Lucero, H. M. Kagan, Lysyl oxidase: An oxidative enzyme and effector of cell function. *Cell. Mol. Life Sci.* **63**, 2304–2316 (2006).

29. L. A. Flanagan, Y.-E. Ju, B. Marg, M. Osterfield, P. A. Janmey, Neurite branching on deformable substrates. *Neuroreport* **13**, 2411–2415 (2002).

30. A. J. Engler, M. A. Griffin, S. Sen, C. G. Bönnemann, H. L. Sweeney, D. E. Discher, Myotubes differentiate optimally on substrates with tissue-like stiffness: Pathological implications for soft or stiff microenvironments. *J. Cell Biol.* **166**, 877–887 (2004).

31. A. J. Garcia, C. D. Reyes, Bio-adhesive surfaces to promote osteoblast differentiation and bone formation. *J. Dent. Res.* **84**, 407–413 (2005).

32. H. J. Kong, T. R. Polte, E. Alsberg, D. J. Mooney, FRET measurements of cell-traction forces and nano-scale clustering of adhesion ligands varied by substrate stiffness. *Proc. Natl. Acad. Sci. U.S.A.* **102**, 4300–4305 (2005).

33. M. J. Paszek, N. Zahir, K. R. Johnson, J. N. Lakins, G. I. Rozenberg, A. Gefen, C. A. Reinhart-King, S. S. Margulies, M. Dembo, D. Boettiger, D. A. Hammer, V. M. Weaver, Tensional homeostasis and the malignant phenotype. *Cancer Cell* **8**, 241–254 (2005).

34. P. L. Toogood, P. J. Harvey, J. T. Repine, D. J. Sheehan, S. N. VanderWel, H. Zhou, P. R. Keller, D. J. McNamara, D. Sherry, T. Zhu, J. Brodfuehrer, C. Choi, M. R. Barvian, D. W. Fry, Discovery of a potent and selective inhibitor of cyclin-dependent kinase 4/6. *J. Med. Chem.* **48**, 2388–2406 (2005).

35. R. S. Fischer, K. A. Myers, M. L. Gardel, C. M. Waterman, Stiffness-controlled three-dimensional extracellular matrices for high-resolution imaging of cell behavior. *Nat. Protoc.* **7**, 2056–2066 (2012).

36. M. A. Serban, G. H. Yang, G. D. Prestwich, Synthesis, characterization and chondroprotective properties of a hyaluronan thioethyl ether derivative. *Biomaterials* **29**, 1388–1399 (2008).

37. M. S. Zhang, S. F. Brunner, N. Huguenin-Dezot, A. D. Liang, W. H. Schmied, D. T. Rogerson, J. W. Chin, Biosynthesis and genetic encoding of phosphothreonine through parallel selection and deep sequencing. *Nat. Methods* **14**, 729–736 (2017).

38. F. Mattiroli, J. H. A. Vissers, W. J. van Dijk, P. Ikpa, E. Citterio, W. Vermeulen, J. A. Marteijn, T. K. Sixma, RNF168 ubiquitinates K13-15 on H2A/H2AX to drive DNA damage signaling. *Cell* **150**, 1182–1195 (2012).

39. M. Xu, B. Skaug, W. W. Zeng, Z. J. Chen, A ubiquitin replacement strategy in human cells reveals distinct mechanisms of IKK activation by TNFα and IL-1β. *Mol. Cell* **36**, 302–314 (2009).

40. Z. P. Meng, T. Moroishi, K.-L. Guan, Mechanisms of Hippo pathway regulation. *Gene Dev.* **30**, 1–17 (2016).

41. J. R. Tse, A. J. Engler, Preparation of hydrogel substrates with tunable mechanical properties. *Curr. Protoc. Cell Biol.* **Chapter 10**, Unit 10.16 (2010).

42. A. J. Engler, L. Richert, J. Y. Wong, C. Picart, D. E. Discher, Surface probe measurements of the elasticity of sectioned tissue, thin gels and polyelectrolyte multilayer films: Correlations between substrate stiffness and cell adhesion. *Surf. Sci.* **570**, 142–154 (2004).

43. R. Nishi, P. W. G. Wijnhoven, Y. Kimura, M. Matsui, R. Konietzny, Q. Wu, K. Nakamura, T. L. Blundell, B. M. Kessler, The deubiquitylating enzyme UCHL3 regulates Ku80 retention at sites of DNA damage. *Sci. Rep.* **8**, 17891 (2018).

44. L. L. Phu, A. Izrael-Tomasevic, M. L. Matsumoto, D. Bustos, J. N. Dynek, A. V. Fedorova, C. E. Bakalarski, D. Arnott, K. Deshayes, V. M. Dixit, R. F. Kelley, D. Vucic, D. S. Kirkpatrick, Improved quantitative mass spectrometry methods for characterizing complex ubiquitin signals. *Mol. Cell. Proteomics* **10**, M110.003756 (2011).

45. M. Deng, X. Yang, B. Qin, T. Liu, H. Zhang, W. Guo, S. B. Lee, J. J. Kim, J. Yuan, H. Pei, L. Wang, Z. Lou, Deubiquitination and activation of AMPK by USP10. *Mol. Cell* **61**, 614–624 (2016).

46. T. Thundat, R. J. Warmack, G. Y. Chen, D. P. Allison, Thermal and ambient-induced deflections of scanning force microscope cantilevers. *Appl. Phys. Lett.* **64**, 2894–2896 (1994).